Effect of titanium substitution and temperature variation on structure and magnetic state of barium hexaferrites

Vinnik D.A., Zhivulin V.E., Uchaev D.A., Gudkova S.A., Zhivulin D.E., Starikov A. Yu, Trukhanov S.V., Turchenko V.A., Zubar T.I., Gavrilov T.P., Eremin R.M., Fadeev E., Lähderanta E., Sombra A.S.B., Zhou D., Jotania R.B., Singh Charanjeet, Trukhanov A.V.

EFFECT OF TITANIUM DOPING AND TEMPERATURE VARIATION ON STRUCTURE AND MAGNETIC STATE OF BARIUM HEXAFERRITE

D.A. Vinnik[1*], V.E. Zhivulin[1], D.A. Uchaev[1], S.A. Gudkova[1], D.E. Zhivulin[1], A.Yu. Starikov[1],

S.V. Trukhanov[2,3], V.A. Turchenko[1,4,5], T.I. Zubar[1,2], T.P. Gavrilova[6], R.M. Eremina[6],

E. Fadeev[7], E. Lähderanta[7], A.S.B. Sombra[8], D. Zhou[9], R.B. Jotania[10], C. Singh[11],

A.V. Trukhanov[1,2,3]

[1]Laboratory of crystal growth, South Ural State University, 454080, Chelyabinsk, Lenin av., 76, Russia

[2]Scientific Practical Materials Research Centre of NAS of Belarus, 220072, Minsk, P. Brovki str., 19, Belorussia, [*]corresponding author e-mail: truhanov@ifttp.bas-net.by

[3]National University of Science and Technology MISiS, 119049, Moscow, Leninsky av., 4, Russia

[4]Frank Laboratory of Neutron Physics, Joint Institute for Nuclear Research, 141980, Dubna, Joliot-Curie str., 6, Russia

[5]Donetsk Institute of Physics and Technology named after O.O. Galkin of the NASU, 03680, Kiev, Nauki av., 46, Ukraine

[6]Zavoisky Physical-Technical Institute, FRC Kazan Scientific Center of RAS, 420029, Kazan, Sibirsky tract, 10/7, Russia

[7]Department of Physics, LUT-University, Lappeenranta, Finland.

[8]Department of Physics, Federal University of Ceara, Fortaleza, Ceara 60-455-970, Brazil

[9]Electronic Materials Research Laboratory, Key Laboratory of the Ministry of Education & International Center for Dielectric Research, School of Electronic Science and Engineering, Xi'an Jiaotong University, Xi'an 710049, China

[10]Department of Physics, Electronics and Space Science, Gujarat University, Gujarat, Ahmedabad 380009, India

[11]School of Electronics and Electrical Engineering, Lovely Professional University, Phagwara, Punjab 144411, India

A number of solid solutions based on $BaFe_{12-x}Ti_xO_{19}$ M-type barium hexaferrite doped with titanium cations up to x = 2.00 were obtained using conventional ceramic technology. The phase composition, crystal structure and unit cell parameters were refined by the Rietveld method using powder X-ray diffraction data up to T = 900 K. It was found that all the compositions have a magnetoplumbite structure satisfactorily described by $P6_3/mmc$ space group (No. 194). With increasing temperature and doping concentration, the unit cell parameters increase almost monotonically. The minimum volume of V ~ 696.72 $Å^3$ was determined for the composition with x = 1.00 at T= 100 K, while the maximum value of V ~ 714.00 $Å^3$ is observed for the composition with x = 2.00 at T= 900 K. The mechanism of occupation nonequivalent crystallographic positions with titanium cations is established. The spin-glass component of the magnetic phase state is fixed. The T_{dif} temperature of the difference between the ZFC-FC curves decreases with an increase in the concentration of titanium cations and the magnetic field from ~ 237.2 K to ~ 44.5 K, while the T_{inf} inflection temperature of the ZFC curve increases from ~ 21.0 K to ~ 23.8 K. With an increase in the doping concentration, both the D_{av} average and D_{max} maximum clusters grow up to ~ 100 nm. As the magnetic field increases above the critical value, the spin-glass component disappears. For compositions with x > 1.00, the magnetization is not saturated in fields up to 6 T. Along with the formation of the spin-glass component, doping with titanium cations for barium hexaferrite lowers the T_C Curie temperature down to T ~ 600 K. The M_s spontaneous and M_r remanent magnetizations, as well as the B_c coercivity, decrease with increasing doping concentration almost monotonically, while the latter has an inflection point at x = 1.00. The minimum values of spontaneous and remanent magnetization, as well as coercivity, are observed for the composition with x = 2.00 and amount to M_s ~ 17.7 emu/g, M_r ~ 1.9 emu/g, and B_c ~ 3.9*10^{-3} T, respectively. An interpretation of the magnetic state of the doped $BaFe_{12-x}Ti_xO_{19}$ barium hexaferrite is given taking into account the mechanism of occupation nonequivalent crystallographic positions with titanium cations.

Keywords: barium hexaferrite; titanium doping; crystal structure; magnetization; spin glass.

1. Introduction

Complex oxides of transition elements are of great applied and scientific importance [1-3]. They find various applications in practice, the main of which are magnetic [4-6], dielectric [7-9], magnetodielectric materials [10-12], energy storage devices [13-15], supercapacitors [16, 17], heating inductors including elements of hyperthermia [18, 19] and much more. Among these complex oxides, iron compounds occupy a dominant role as materials for microwave devices [20-22]. The $AFe_{12}O_{19}$ (A = Sr, Ba) M-type hexaferrites are of particular practical importance due to the high values of the T_C Curie temperature, m_{tot} total magnetic moment, and k_a coefficient of magnetic crystallographic anisotropy [23].

The $BaFe_{12}O_{19}$ M-type barium hexaferrite has a crystal structure of magnetoplumbite with a hexagonal symmetry of the unit cell, which is more often described by $P6_3/mmc$ space group (No. 194) [24]. Fe^{3+} iron cations with a spin magnetic moment of $S = 5\,\mu_B$ are located in 5 nonequivalent crystallographic positions with the corresponding multiplicities: $1\times2a$, $2\times4f_{vi}$, $6\times12k$ (octahedral positions); $1\times2b$ (pentahedral position) and $2\times4f_{iv}$ (octahedral position). Magnetic moments, ordering in accordance with the Gorter model $mtot = 1*m(2a) + 1*m(2b) - 2*m(4f_{iv}) - 2*m(4f_{vi}) + 6*m(12k)$, can lead to the formation of the total magnetic moment equal to $20\,\mu_B$ in the ground state [25].

The doping of the $BaFe_{12-x}M_xO_{19}$ barium hexaferrite with various $M = Al^{3+}$, Sc^{3+}, In^{3+} etc. chemical elements is an effective way to control its physicochemical properties [26]. At least three types of doping can be distinguished: charge, spin, and mixed doping. With the first type of doping, the charge state of the iron cations changes, and with the second, the spin state of iron cations changes. The third type of doping is characterized by a simultaneous change in the charge and spin states of iron cations. The heterovalent doping of the Fe^{3+} iron cations with the diamagnetic Ti^{4+} (S = 0) titanium cations is of the mixed type. As a result of this process, Fe^{2+} iron cations are formed in different nonequivalent crystallographic positions, which have two characteristic features in barium hexaferrite. First, in the octahedral coordination, the Fe^{2+} iron cation can undergo a spin transition (HS $\rightarrow$ LS) from the high spin state (HS, S = 2) to the low spin state (LS, S = 0) with decreasing temperature [27]. Second, in the tetrahedral coordination, the Fe^{2+} iron

cation is Jahn–Teller one, which can manifest itself at an appropriate concentration in the anisotropic distortion of polyhedra [28].

The $BaFe_{12-x}T_xO_{19}$ titanium-doped barium hexaferrites are of undoubted interest as materials for microwave absorption [29–39]. It was previously found that for the composition with x = 0.25 the S_{11} reflection coefficient reaches ~ -80 dB at frequency of f ≈ 10.5 GHz, and for the composition with x = 1.00 the C_{21} transmission coefficient exceeds > -60 dB at frequency of f ≈ 12 GHz [34]. The transmission coefficient for the composition with x = 0.50 exceeds > -40 dB at frequency of f ≈ 9.3 GHz [37]. In order to achieve the desired amplitude-frequency characteristics, it is necessary to know the features of the magnetic and electric phase states of the compositions used and to controllably change such magnetic parameters as the Curie temperature, spontaneous magnetization and anisotropy field, and such electrical parameters as ac-resistivity and permeability. Earlier, some results on the study of the magnetic phase state of titanium-doped solid solutions have already been obtained [40].

For the $BaFe_{12-x}Ti_xO_{19}$ (x ≤ 1) barium hexaferrite ceramics the crystal structure and magnetodielectric properties have been investigated. It was established that titanium cations are predominantly occupied the $4f_{IV}$, $4f_{VI}$ and 12k positions. The noncollinear magnetic structure is founded at low temperature. The M_s saturation magnetization decreases down to ~ 56.7 emu/g with increasing x up to 1.00. The M_r residual magnetization and B_c coercivity decrease also. The ac-resistivity decreases with increasing x substitution level up to 1.00 and f frequency up to 10^5 Hz. The real part of the dielectric constant for the x = 0.50 gradually decreases at heating up to ~ 500 K, after which it begins to increase sharply. The dielectric loss tangent for this sample has a maximum in the region of ~ 500 K [40].

In the present work, the range of solid solutions of titanium-doped barium hexaferrites was expanded up to 2.00. The phase composition, crystal structure, and unit cell parameters were refined by the Rietveld method based on powder X-ray diffraction data in a wide temperature range. The doping mechanism has been studied. The features of the magnetic phase state are

investigated. The spin-glass component is fixed. The spontaneous magnetization and coercivity are measured at room temperature.

2. Experimental

The high purity Fe_2O_3 (99.999%) and TiO_2 (99.999%) oxides and $BaCO_3$ (99.99%) carbonate have been used to prepare the doped $BaFe_{12-x}Ti_xO_{19}$ (x = 0.25; 0.50; 0.75; 1.00; 1.25; 1.50 and 2.00) samples using conventional ceramic technology. Firstly, the oxides and carbonate have been weighted with design ratio and thoroughly mixed in molar proportions in an agate mortar. Then, the chemical mixtures were ground in a ball mill for 10 hs with a small amount of ethyl alcohol. Then the calcination has been performed at 1200°C in air during 6 h to obtain the magnetoplumbite phase. Final synthesis was carried out at 1300°C in air during 6 h. After synthesis the sample has been slowly cooled (100°C*h^{-1}) [40]. The formation of $BaFe_{12-x}Ti_xO_{19}$ powders can be represented as follows:

$$BaCO_3 + \left(\frac{12-x}{2}\right)Fe_2O_3 + (x)\,TiO_2 \rightarrow BaFe_{12-x}Ti_xO_{19} + CO_2 \uparrow + \frac{1}{4}xO_2 \uparrow \qquad (1)$$
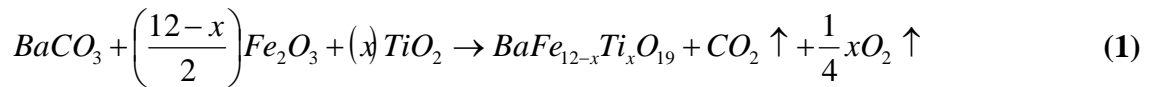
The chemical phase content, crystal structure and unit cell parameters were refined by Rietveld analysis [41] using the FullProf [42]. X-ray diffractometer EMPYREAN (PANalytical firm) with Cu-K$_\alpha$ radiation $\lambda = 1.541874$ Å was used to collect the experimental data up to 900 K [43]. The powder diffraction software package HighScore Plus [44] which includes the standards of the ICDD [45] was applied.

Temperature dependence of specific magnetization in zero field cooled (ZFC) and field cooled (FC) regimes was measured up to T = 400 K and B = 2 T fields by Liquid Helium Free High Field Measurement System (VSM) [46]. Field dependence of specific magnetization was measured at 300 K [47].

The high temperature ESR investigations were performed on the Varian E12 spectrometer at the frequency of 9.36 GHz (X-band) in the temperature range from 292 K to 680 K.

3. Results and discussion

The experimental X-ray diffraction data and fitting lines for some of the obtained compositions are shown in Fig. 1. To refine the atomic coordinates and unit cell parameters, the $P6_3/mmc$ (No. 194) space group [48] was used, which gave satisfactory results. The χ^2 goodness fitting parameter did not exceed ~ 2.5. Fig. 1 shows that the difference curve contains small maxima. Bragg reflections are slightly shifted towards smaller angles with increasing temperature, which generally corresponds to an increase in an interplanar distance. The diffraction pattern does not fundamentally change, which indicates the absence of sharp structural changes.

The lattice constants a, c and the volume V of the unit cell depend on doping concentration as shown in Fig. 2. In general, they increase with x. The lattice constant c increases monotonically. Moreover, the rate of change of the lattice constant c $dc/dx \approx 11*10^{-2}$ Å/x at a high temperature is higher than those $dc/dx \approx 7.5*10^{-2}$ Å/x at a low temperature. The dependence of the lattice constant a and volume V is characterized by extrema. A local minimum is observed in these dependences in the temperature range 100-300 K at x = 1.00. At a high temperature of 900 K, these dependences have a local minimum at x = 0.50 and a local maximum at x = 1.25. The volume V also changes at a higher rate of $dV/dx \approx 3.3$ Å^3/x at high temperatures than those $dV/dx \approx 2.2$ Å^3/x at low temperatures.

The temperature dependences of the lattice constants a and c and volume V of the unit cell for different doping concentrations are shown in Fig. 3. All quantities change almost monotonically with increasing temperature. An anomaly is observed for the composition with x = 1.00 at 300 K. The minimum value of the lattice constant a ≈ 5.883 Å is observed for the composition with x = 1.00 at 100 K. The maximum value of the lattice constant a ≈ 5.923 Å is observed for the composition with x = 1.00 at 900 K. For the same composition with x = 1.00, the highest $da/dT \approx 5.0*10^{-5}$ Å/K change rate of the lattice constant a is observed with increasing temperature. The minimum value of the lattice constant c ≈ 23.20 Å is observed for the composition with x = 0.25 at 100 K. The maximum value of the lattice constant c ≈ 23.55 Å is observed for the composition with x = 2.00 at 900 K. With an increase in the doping concentration from x = 0.25

to x = 2.00, the rate of change of the lattice constant c increases from $dc/dT \approx 2.1*10^{-4}$ Å/K to $dc/dT \approx 2.6*10^{-4}$ Å/K, respectively. The maximum rate of change in the lattice constant c $dc/dT \approx 2.9*10^{-4}$ Å/K is observed for the composition with x = 1.00. The change rate of volume V increases from $dV/dT \approx 1.1*10^{-2}$ Å³/K for x = 0.25 to $dV/dT \approx 1.7*10^{-2}$ Å/K for x = 2.00 with a maximum $dV/dT \approx 2.1*10^{-2}$ Å/K for x = 1.00.

It is clearly seen from the Figs. 2 and 3 that the relative change in the a parameter is much less than the relative change in the c parameter. For example, the relative change in the a parameter vs. x at the room temperature is ~ $1.7*10^{-3}$ % and vs. T for the x = 1.00 is ~ $6.8*10^{-3}$ %, whereas the relative change in the c parameter vs. x at the room temperature is ~ $5.8*10^{-3}$ % and vs. T for the x = 1.00 is ~ $10.0*10^{-3}$ %. Such behavior is explained by the high crystal anisotropy of hexaferrite and the peculiarities of the occupation mechanism of nonequivalent crystallographic positions with the Ti^{4+} titanium cations. The different behavior of the a and c parameters corresponds to the accuracy of the X-ray diffraction measurement.

The behavior of the lattice constants a and c and volume V of the unit cell is explained by a change in the charge and spin state of the $Fe^{2+/3+}$ iron cations and by the mechanism of occupation of the nonequivalent crystallographic positions with the Ti^{4+} titanium cations. Cations of triply Fe^{3+} and doubly Fe^{2+} charged iron in octahedral coordination can be in both low spin (LS) and high spin (HS) states, while in tetrahedral coordination they can only be in high spin (HS) state. According to the data of [49], the following ionic radii can exist in the titanium-doped $BaFe_{12-x}M_xO_{19}$ composition of the barium hexaferrite: fourfold charged Ti^{4+}[IV] titanium cation in tetrahedral coordination $r(Ti^{4+}[IV]) = 0.560$ Å; fourfold charged Ti^{4+}[VI] titanium cation in octahedral coordination $r(Ti^{4+}[VI]) = 0.745$ Å; HS triply charged Fe^{3+}[IV, HS] iron cation in tetrahedral coordination $r(Fe^{3+}[IV, HS]) = 0.630$ Å; LS triply charged Fe^{3+}[VI, LS] iron cation in octahedral coordination $r(Fe^{3+}[VI, HS]) = 0.690$ Å; HS triply charged Fe^{3+}[VI, HS] iron cation in octahedral coordination $r(Fe^{3+}[VI, HS]) = 0.785$ Å; HS doubly charged Fe^{2+}[IV, HS] iron cation in tetrahedral coordination $r(Fe^{2+}[IV, HS]) = 0.770$ Å; LS doubly charged Fe^{2+}[VI, LS] iron cation

in octahedral coordination $r(Fe^{2+}[VI, LS]) = 0.750$ Å; HS doubly charged $Fe^{2+}[VI, HS]$ iron cation in octahedral coordination $r(Fe^{2+}[VI, HS]) = 0.920$ Å.

The concentration dependence of the lattice constants a and c and volume V of the unit cell is explained by the specific mechanism of occupation of the five nonequivalent crystallographic positions 2a, 2b, $4f_{IV}$, $4f_{VI}$ and 12r with the Ti^{4+} titanium cations. The entire doping interval can be divided into three subintervals. In the first doping subinterval, at $x \leq 0.25$, the Ti^{4+} titanium cations replace HS triply charged $Fe^{3+}[VI, HS]$ iron cations in the octahedral positions 2a, $4f_{VI}$ and 12K with the total size effect of $\Delta r(Ti^{4+}[VI] \rightarrow Fe^{3+}[VI, HS]) = -0.040$ Å. The HS doubly charged $Fe^{2+}[IV, HS]$ iron cations appear instead of the triply charged $Fe^{3+}[IV, HS]$ ones in tetrahedral positions $4f_{IV}$ with the size effect of $\Delta r(Fe^{2+}[IV, HS] \rightarrow Fe^{3+}[IV, HS]) = 0.140$ Å. As a result of this occupation, the total size effect is $\delta r(1) = \Delta r(Fe^{2+}[IV, HS] \rightarrow Fe^{3+}[IV, HS]) + \Delta r(Ti^{4+}[VI] \rightarrow Fe^{3+}[VI, HS]) = 0.100$ Å. In the second doping subinterval $0.25 < x \leq 1.00$, the fourfold charged $Ti^{4+}[IV]$ titanium cations replace the HS doubly charged $Fe^{2+}[IV, HS]$ iron cations in the $4f_{IV}$ tetrahedral positions with the size effect of $\Delta r(Ti^{4+}[IV] \rightarrow Fe^{2+}[IV, HS]) = -0.210$ Å. The HS doubly charged $Fe^{2+}[VI, HS]$ iron cations appear instead of the HS triply charged $Fe^{3+}[VI, HS]$ iron cations in the octahedral 2a, $4f_{VI}$ and 12K positions with the size effect of $\Delta r(Fe^{2+}[VI, HS] \rightarrow Fe^{3+}[VI, HS]) = 0.135$ Å. As a result of this occupation, the total size effect is $\delta r(2) = \Delta r(Ti^{4+}[IV] \rightarrow Fe^{2+}[IV, HS]) + \Delta r(Fe^{2+}[VI, HS] \rightarrow Fe^{3+}[VI, HS]) = -0.075$ Å. In the third doping interval, $1.00 < x \leq 2.00$, the fourfold charged $Ti^{4+}[VI]$ titanium cations replace the HS triply charged $Fe^{3+}[VI, HS]$ iron cations in octahedral 2a, $4f_{VI}$ and 12K positions with the size effect of $\Delta r(Ti^{4+}[VI] \rightarrow Fe^{3+}[VI, HS]) = -0.040$ Å. The HS doubly charged $Fe^{2+}[VI, HS]$ iron cations appear instead of the HS triply charged $Fe^{3+}[VI, HS]$ cations in the octahedral 2a, $4f_{VI}$ and 12K positions with the size effect of $\Delta r(Fe^{2+}[VI, HS] \rightarrow Fe^{3+}[VI, HS]) = 0.135$ Å. As a result of this occupation, the total size effect is $\delta r(3) = \Delta r(Ti^{4+}[VI] \rightarrow Fe^{3+}[VI, HS]) + \Delta r(Fe^{2+}[VI, HS] \rightarrow Fe^{3+}[VI, HS]) = 0.095$ Å. This occupation mechanism is in good agreement with the previously proposed one [40].

As we have already noted above, at three concentration subintervals, features are observed in the occupation of the nonequivalent crystallographic positions by the Ti^{4+} titanium cations. An increase in the average cationic radius in the B-sublattice of hexaferrite leads to an increase in the volume of the generalized oxygen polyhedron. The total size effect $\delta r(1) + \delta r(2) + \delta r(3) = 0.120$ Å over the entire doping range is positive; therefore, the lattice broadening is observed in general, and hence the interplanar distance increases. This type of doping leads to an increase in interplanar spacing as a trend.

Taking into account such occupation mechanism, the nonmonotonic behavior of the concentration dependence of the lattice constant a and volume V of the unit cell in Fig. 2 at 300 K is understandable. Recalling that the HS doubly charged Fe^{2+}[IV, HS] iron cation in tetrahedral coordination is a Jahn-Teller cation, one can understand the monotonic change in the c parameter of unit cell. At low temperatures, the doubly charged Fe^{2+}[VI, HS] iron cations in octahedral coordination can undergo a transition to the LS state Fe^{2+}[VI, HS] $\rightarrow Fe^{2+}$[VI, LS] [27], which will be seen somewhat below. With an increase in temperature, the lattice constants a and c and volume V, as it can be seen from Fig. 3, undergo a monotonic increase due to an increase in the energy of the chaotic vibrational motion of cations.

Indeed, it is well known that 3-d transition metals can have a mixed charge state. Since the titanium atom is in the 4-th group of the periodic table, this indicates that the main charge state is 4+. This behavior is easily explained by the filling of electron orbitals and the binding energy of 3-d electrons. The authors do not have access to information about the works in which triple-charged Ti^{3+} titanium cations in complex transition metal oxides were observed. Based on this fact, when considering the occupation mechanism and interpreting the magnetic properties, the presence of triple-charged charged Ti^{3+} titanium cations was not taken into account. With the appearance of oxygen vacancies, it is most likely that triple-charged Fe^{3+} iron cations will transform into double-charged Fe^{2+} ones, rather than four-charged Ti^{4+} titanium cations will transform into triple-charged Ti^{4+} ones. Presumably, triple-charged Ti^{3+} titanium cations will lead to a greater increase in the unit cell volume and interplanar distance.

The temperature dependence of the ZFC and FC magnetization in the weak field of 0.01 T is shown in Fig. 4. It is clearly seen that with an increase in the doping concentration, the signal is ~ 2.4 emu / g for the x = 0.25 and it gradually decreases. All the ZFC curves start almost from zero and reach saturation above ~ 180 K. The FC curves are practically constant. The difference between the ZFC and FC curves indicates the existence of a frustrated component of the magnetic phase state [50]. This is the so-called spin glass state. As a rule, in the case of a classical spin glass, two characteristic temperatures are distinguished. These are the T_f freezing temperature and the T_{dif} difference temperature. Both these temperatures characterize the size of the magnetically disordered cluster. The spin glass state arises as a result of frustration of exchange interactions, and, in some approximation, it can be considered as a superposition of the ordered clusters located in a disordered matrix. If the order parameter exceeds a certain critical value, then on the contrary, one speaks of disordered clusters located in an ordered matrix. The peak temperature of the ZFC curve, the T_f freezing temperature, determines the average cluster size according to the Bean – Livingstone ratio [51]. The T_{dif} difference temperature between the ZFC and FC curves characterizes the maximum cluster size. The T_{dif} difference temperature decreases from ~ 237.2 K to ~ 164.0 K with an increase in the concentration of titanium cations and the magnetic field. From the data presented in Fig. 4 it is well seen that the maximum cluster size decreases at the rate $dT_{dif}/dx \approx$ -36.61 K/x.

The fact of the linear decrease in the T_{dif} difference temperature indicates a decrease in the maximum size of the ordered cluster. This happens because the intensity of the $Fe^{2+/3+}$ - O^{2-} - T^{4+} indirect superexchange interactions become negative and the Fe^{3+} - O^{2-} - Fe^{3+} positive exchange-linked chains are broken as a result of doping with titanium cations. With a uniform distribution of substitutional titanium cations over the lattice, a decrease in the maximum size of the ordered cluster will be observed.

As it was mentioned above, the T_f freezing temperature is determined by the peak position of the ZFC curve. From Fig. 4 it is well seen that the ZFC curves increase monotonically and have no peak. However, they can be characterized by a similar inflection point temperature. The T_{inf}

inflection temperature is determined by the local extremum point on the first derivative of the corresponding curve. Fig. 5 shows the temperature dependences of the first derivative of the ZFC curve in the field of 0.01 T. It can be seen that the T_{inf} inflection point temperature increases monotonically and nonlinearly. The T_{inf} inflection point temperature increases from ~ 21.0 K to ~ 23.8 K. Above x > 1.00, the dependence reaches saturation. Hence, we can conclude that, in the field of 0.01 T, the average size of ordered cluster increases at rate of d $T_{inf}/dx \approx 2.55$ K/x in the x range of 0.00 - 1.00 and d $T_{inf}/dx \approx 0.27$ K/x in the x range of 1.00 - 2.00. With increase in the doping concentration, both the D_{av} average and D_{max} maximum clusters grow up to ~ 100 nm [47].

An increase in the field up to 1 T does not lead to a fundamental change in the magnetic phase state. The magnetization becomes much higher and amounts to ~ 68.5 emu/g for x = 0.25 at low temperatures. The extended temperature range of coincidence of the ZFC and FC curves indicates a homogeneous ferrimagnetic state. A pronounced magnetic transition appears in the region of ~ 300 K. The T_{dif} difference temperature also decreases with an increase in the doping concentration. As it is seen from Fig. 6, the rate of decrease in the maximum cluster size in this case becomes lower and amounts to $dT_{dif}/dx \approx -62.43$ K/x.

It should be noted here that the low-temperature drop in the magnetization in this case is most likely a consequence of a change in the magnetic structure, and it is not cluster behavior, since the field amount is too high. This behavior can be explained by the formation of a noncollinear ferrimagnetic structure as a result of the spin transition of the doubly charged Fe^{2+} iron cation from LS to HS state (LS $\rightarrow$ HS) with increasing temperature [52]. This behavior is often observed for doubly charged Fe^{2+} iron cations in metal-organic complexes [53]. To clarify the features of the magnetic structure under these conditions, it is necessary to carry out neutron diffraction experiments, which are planned in the very near future and will be performed at the IBR-2M reactor at JINR (Dubna, Russia). With an increase in the field to 2 T, the difference between the ZFC and FC curves disappears, as does the low-temperature anomaly, which can be seen from the data in Fig. 7.

With an increase in the doping concentration, the M_s spontaneous magnetization decreases monotonically, which can be seen from Fig. 8. At the room temperature, the magnetization in the field of 6 T is ~ 74.83 emu/g for the $x = 0.00$, while for the $x = 2.00$ it is ~ 29.22 emu/g. The field dependences for the $x \geq 1.25$ are not saturated in the fields up to 6 T. The M_r remanent magnetization and B_c coercivity also decrease monotonically with an increase in the doping concentration, which is clearly seen from the more detailed Fig. 9. The change in magnetic parameters is satisfactorily described by the change in the charge and spin state of the $Fe^{2+/3+}$ iron cations and by the mechanism of the occupation by the T^{4+} titanium cations the nonequivalent crystallographic positions as it was proposed above.

The M_s spontaneous and M_r remanent magnetization decrease mainly for two reasons. The first reason is the appearance of diamagnetic Ti^{4+} titanium cationes mainly in the 2a and 12k octahedral positions. Since the diamagnetic cation has a local spin equal to zero, the total moment will decrease with an increase in the doping concentration. One Ti^{4+} titanium cation converts one trivalent Fe^{3+} iron cation with a local spin of 5 μ_B into a bivalent Fe^{2+} iron cation with a local spin of 4 μ_B. Such a transformation in general will also reduce the total moment and hence the M_s spontaneous and M_r remanent magnetization.

The decrease in the B_c coercivity upon titanium doping can also be explained by a decrease in the intensity and stiffness of the $Fe^{2+/3+}$ - O^{2-} - T^{4+} indirect superexchange interactions as compared to the Fe^{3+} - O^{2-} - Fe^{3+} initial interactions. A decrease in the stiffness leads to an increased susceptibility of local spins to the reorienting action of the weak fields, as a result of which, when the direction of the field is changed, the demagnetizing effect quickly reaches a maximum, and the magnetization becomes zero.

The doping with diamagnetic Ti^{4+} titanium cations leads to a significant weakening of the $Fe^{3+}(Ti^{4+})$ – O^{2-} - $Fe^{3+}(Fe^{2+})$ exchange interactions and a decrease in the T_C Curie temperature. Typical electron spin resonance (ESR) spectra of the investigated $BaFe_{10.5}Ti_{1.5}O_{19}$ sample are presented in Fig. 10. In the temperature range above ~ 650 K the experimental spectrum consists of one ESR line with the Lorentzian lineshape. We suggest that the sample is a paramagnetic at

this temperatures and the exchange-narrowing line is due to the signal from iron spins with strong exchange interaction. In the temperature range below ~ 650 K the experimental spectrum has a complex lineshape. One can suggest that lines of ferromagnetic resonance were detected in magnetic resonance spectra below ~ 650 K. The observation of several lines in the ferromagnetic resonance spectrum may be related to the phase ordering of spin sublattices of the $Fe^{2+/3+}$ iron cations which occupy 12 different crystallographic positions and the complex nature of the $Fe^{3+}(Ti^{4+}) - O^{2-} - Fe^{3+}(Fe^{2+})$ exchange interactions between these cations.

Despite the fact that the decomposition/interpretation of the magnetic resonance spectrum is rather difficult task in this case, the integral intensity of ESR absorption line can be obtained by double integration of the original signal (Fig. 11). It should be noted that the integral intensity of the ESR absorption line is proportional to the concentration of magnetic centers and magnetic moment of the sample. One can see from Fig. 11 that the temperature dependance of the integral intensity demonstrates the stepwise behavior which is typical for the ferromagnetic state near the T_C Curie temperature. The T_C Curie temperature can be obtained as the minimun in the temperature dependance of the first derivative of the integral intensity with respect to temperature (dI_{int}/dT vs. T). And it is equal $T_C \approx 610$ K.

The concentration dependences of the M_s spontaneous magnetization, M_r remanent magnetization and B_c coercivity are shown in Fig. 12. With an increase in the doping concentration, the M_s spontaneous magnetization decreases monotonically but nonlinearly from a maximum value of ~ 74.31 emu/g for the x = 0.00 to ~ 17.65 emu/g for the x = 2.00. The change rate is $dM_s/dx \approx$ -28.33 emu*g^{-1}*x^{-1}. The M_r remanent magnetization also decreases monotonically from ~ 26.92 emu/g for the x = 0.00 to ~ 1.86 emu/g for the x = 2.00 at the rate of $dM_r/dx \approx$ -12.53 emu*g^{-1}*x^{-1}. The B_c coercivity decreasing from ~ 35.37 mT for the x = 0.00 to ~3.91 mT for the x = 2.00 has an inflection point at the x = 1.00. The change rate is $dB_c/dx \approx$ -15.73 mT*x^{-1}.

Conclusions

The titanium doped $BaFe_{12-x}Ti_xO_{19}$ (x = 0.25; 0.50; 0.75; 1.00; 1.25; 1.50 and 2.00) M-type barium hexaferrite solid solutions were obtained using conventional ceramic technology. The phase composition, crystal structure and unit cell lattice constants were refined by the Rietveld method using powder XRD data up to T = 900 K. The χ^2 goodness fitting parameter did not exceed ~ 2.5. It was found that all the compositions have a magnetoplumbite structure satisfactorily described by $P6_3/mmc$ space group (No. 194). With increasing temperature and doping concentration, the unit cell parameters increase almost monotonically. The rate of change of the lattice constant c $dc/dx \approx 11*10^{-2}$ Å/x at a high temperature is higher than those $dc/dx \approx 7.5*10^{-2}$ Å/x at a low temperature. The minimum volume of V ~ 696.72 $Å^3$ was determined for the composition with x = 1.00 at T= 100 K, while the maximum value of V ~ 714.00 $Å^3$ is observed for the composition with x = 2.00 at T= 900 K. The volume V also changes at a higher rate of $dV/dx \approx 3.3$ $Å^3$/x at high temperatures than those $dV/dx \approx 2.2$ $Å^3$/x at low temperatures. For the same composition with x = 1.00, the highest $da/dT \approx 5.0*10^{-5}$ Å/K change rate of the lattice constant a is observed with increasing temperature. The rate of change of the lattice constant c increases from $dc/dT \approx 2.1*10^{-4}$ Å/K to $dc/dT \approx 2.6*10^{-4}$ Å/K for the x = 0.25 to x = 2.00, respectively. The change rate of volume V increases from $dV/dT \approx 1.1*10^{-2}$ $Å^3$/K for x = 0.25 to $dV/dT \approx 1.7*10^{-2}$ Å/K for x = 2.00 with a maximum $dV/dT \approx 2.1*10^{-2}$ Å/K for x = 1.00. The mechanism of occupation nonequivalent crystallographic positions with titanium cations is established. The entire $0.00 \leq x \leq 2.00$ doping interval can be divided into three subintervals: 1). $x \leq 0.25$, 2). $0.25 < x \leq 1.00$ and 3). $1.00 < x \leq 2.00$. Next type of occupation are established: 1). Fe^{2+}[IV, HS] $\rightarrow Fe^{3+}$[IV, HS] and Ti^{4+}[VI] $\rightarrow Fe^{3+}$[VI, HS]; 2). Ti^{4+}[IV] $\rightarrow Fe^{2+}$[IV, HS] and Fe^{2+}[VI, HS] $\rightarrow Fe^{3+}$[VI, HS] and 3). Ti^{4+}[VI] $\rightarrow Fe^{3+}$[VI, HS] and Fe^{2+}[VI, HS] $\rightarrow Fe^{3+}$[VI, HS]. The spin-glass component of the magnetic phase state is fixed. The T_{dif} difference temperature between the ZFC-FC curves decreases with an increase in the concentration of titanium cations and the magnetic field from ~ 237.2 K to ~ 44.5 K, while the T_{inf} inflection point temperature of the ZFC curve increases from ~ 21.0 K to ~ 23.8 K. The maximum cluster size decreases at the rate $dT_{dif}/dx \approx -36.61$ K/x. In the field of 0.01 T, the average size of ordered cluster increases at

rate of d $T_{inf}/dx \approx 2.55$ K/x in the x range of 0.00 - 1.00 and d $T_{inf}/dx \approx 0.27$ K/x in the x range of 1.00 - 2.00. With an increase in the doping concentration, both the D_{av} average and D_{max} maximum clusters grow up to ~ 100 nm. The change in the magnetic structure at low temperature in field of 1 T was established, and it is explained by the formation of a noncollinear ferrimagnetic structure as a result of the spin transition of the doubly charged Fe^{2+} iron cation from LS to HS state (LS $\rightarrow$ HS) with increasing temperature. As the magnetic field increases above the critical value, the spin-glass component disappears. At the room temperature, the magnetization in field of 6 T is ~ 74.83 emu/g for the x = 0.00, while for the x = 2.00 it is ~ 29.22 emu/g. For compositions with x > 1.00, the magnetization is not saturated in fields up to 6 T. Along with the formation of the spin-glass component, doping with titanium cations for the barium hexaferrite lowers the T_C Curie temperature down to T ~ 600 K. The M_s spontaneous and M_r remanent magnetizations, as well as the B_c coercivity, decrease with increasing doping concentration almost monotonically, while the latter has an inflection point at x = 1.00. The minimum values of spontaneous and remanent magnetization, as well as coercivity, are observed for the composition with x = 2.00 and amount to M_s ~ 17.7 emu/g, M_r ~ 1.9 emu/g, and B_c ~ $3.9*10^{-3}$ T, respectively. An interpretation of the magnetic state of the doped $BaFe_{12-x}Ti_xO_{19}$ barium hexaferrite is given taking into account the mechanism of occupation nonequivalent crystallographic positions with titanium cations. Doping of titanium cations for the barium hexaferrite leads to a controlled change in the magnetic properties of the compound and makes it promising for microwave applications.

Acknowledgment

References

1. J. Chen, J.E. Daniels, J. Jian, Z. Cheng, J. Cheng, J. Wang, Q. Gu, S. Zhang, Origin of large electric-field-induced strain in pseudo-cubic $BiFeO_3$–$BaTiO_3$ ceramics, Acta Mater. 197 (2020) 1-9. https://doi.org/10.1016/j.actamat.2020.07.032.

2. S.L. Wachowski, I. Szpunar, M.H. Sørby, A. Mielewczyk–Gryń, M. Balaguer, C. Ghica, M.C. Istrate, M. Gazda, A.E. Gunnæs, J.M. Serra, T. Norby, R. Strandbakke, Structure and water uptake in $BaLnCo_2O_{6−δ}$ (Ln =La, Pr, Nd, Sm, Gd, Tb and Dy), Acta Mater. 199 (2020) 297-310. https://doi.org/10.1016/j.actamat.2020.08.018.

3. X. Lv, N. Zhang, J. Wu, X.X. Zhang, The role of adding $Bi_{0.5}A_{0.5}ZrO_3$ in affecting orthorhombic-tetragonal phase transition temperature and electrical properties in potassium sodium niobate ceramics, Acta Mater. 197 (2020) 224-234. https://doi.org/10.1016/j.actamat.2020.07.053.

4. S.V. Trukhanov, Peculiarities of the magnetic state in the system $La_{0.70}Sr_{0.30}MnO_{3-γ}$ ($0 \leq γ \leq 0.25$), JETP 100 (2005) 95-105. https://doi.org/10.1134/1.1866202.

5. S.V. Trukhanov, V.A. Khomchenko, D.V. Karpinsky, M.V. Silibin, A.V. Trukhanov, L.S. Lobanovsky, H. Szymczak, C.E. Botez, I.O. Troyanchuk, A-site ordered state in manganites with perovskite-like structure based on optimally doped compounds $Ln_{0.70}Ba_{0.30}MnO_3$ (Ln = Pr, Nd), J. Rare Earths 37 (2019) 1242-1249. https://doi.org/10.1016/j.jre.2018.12.010.

6. D.V. Karpinsky, M.V. Silibin, S.V. Trukhanov, A.V. Trukhanov, A.L. Zhaludkevich, S.I. Latushka, D.V. Zhaludkevich, V.A. Khomchenko, D.O. Alikin, A.S. Abramov, T. Maniecki, W. Maniukiewicz, M. Wolff, V. Heitmann, A.L. Kholkin, Peculiarities of the crystal structure evolution of $BiFeO_3$–$BaTiO_3$ ceramics across structural phase transitions, Nanomaterials-Basel 10 (2020) 801-12. https://doi.org/10.3390/nano10040801.

7. R.G.M. Oliveira, D.C. Souza, J.E.V. de Morais, G.S. Batista, M.A.S. Silva, D.X. Gouveia,·S. Trukhanov, A. Trukhanov, L. Panina, C. Singh, D. Zhou, A.S.B. Sombra, High thermal stability of RF dielectric properties of $BiVO_4$ matrix with added ZnO, J. Mater. Sci.: Mater. Electron. 31 (2020) 13078–13087. https://doi.org/10.1007/s10854-020-03858-x.

8. D. Wang, B. Siame, S. Zhang, G. Wang, X. Ju, J. Li, Z. Lu, Y. Vardaxoglou, W. Whittow, D. Cadman, S. Sun, D. Zhou, K. Song, I.M. Reaney, Direct integration of cold sintered, temperature-stable $Bi_2Mo_2O_9$-K_2MoO_4 ceramics on printed circuit boards for satellite navigation antennas, J. Eur. Ceram. Soc. 40 (2020) 4029-4034. https://doi.org/10.1016/j.jeurceramsoc.2020.04.025.

9. S.-Z. Hao, D. Zhou, F. Hussain, W.-F. Liu, J.-Z. Su, D.-W. Wang, Q.-P. Wang, Z.-M. Qi, C. Singh, S. Trukhanov, Structure, spectral analysis and microwave dielectric properties of novel $x(NaBi)_{0.5}MoO_4$-$(1-x)Bi_{2/3}MoO_4$ (x = 0.2 - 0.8) ceramics with low sintering temperatures, J. Eur. Ceram. Soc. 40 (2020) 3569-3576. https://doi.org/10.1016/j.jeurceramsoc.2020.03.074.

10. D.A. Vinnik, F.V. Podgornov, N.S. Zabeivorota, E.A. Trofimov, V.E. Zhivulin, A.S. Chernukha, M.V. Gavrilyak, S.A. Gudkova, D.A. Zherebtsov, A.V. Ryabov, S.V. Trukhanov, T.I. Zubar, L.V. Panina, S.V. Podgornaya, M.V. Zdorovets, A.V. Trukhanov, Effect of treatment conditions on structure and magnetodielectric properties of barium hexaferrites, J. Magn. Magn. Mater. 498 (2020) 166190. https://doi.org/10.1016/j.jmmm.2019.166190.

11. S. Sharma, P. Yanda, P. Yadav, I. da Silva, A. Sundaresan, Suppression of long-range ordering and multiferroicity in Sr-substituted $Ba_{3-x}Sr_xMnNb_2O_9$ (x = 1 and 3), J. Magn. Magn. Mater. 512 (2020) 166990. https://doi.org/10.1016/j.jmmm.2020.166990.

12. C.M. Zhu, G.B. Yu, L.G. Wang, M.W. Yao, F.C. Liu, W.J. Kong, Dielectric relaxation and magnetodielectric effect in the spinel $NiCr_2O_4$, J. Magn. Magn. Mater. 506 (2020) 166803. https://doi.org/10.1016/j.jmmm.2020.166803.

13. M. Liu, P. Zhang, Z. Qu, Y. Yan, C. Lai, T. Liu, S. Zhang, Nat. Commun. 10 (2019) 3917. https://doi.org/10.1038/s41467-019-11925-z.

14. P.-J. Wang, D. Zhou, H.-H. Guo, W.-F. Liu, J.-Z. Su, M.-S. Fu, C. Singh, S. Trukhanov, A. Trukhanov, Ultrahigh enhancement rate of energy density of flexible polymer nanocomposites by core-shell $BaTiO_3$@MgO structures as fillers, J. Mater. Chem. A 8 (2020) 11124-11132. https://doi.org/10.1039/d0ta03304a.

15. P.-J. Wang, D. Zhou, J. Li, L.-X. Pangc, W.-F. Liu, J.-Z. Su, C. Singh, S. Trukhanov, A. Trukhanov, Significantly enhanced electrostatic energy storage performance of P(VDF-HFP)/$BaTiO_3$-Bi($Li_{0.5}Nb_{0.5}$)O_3 nanocomposites, Nano Energy 78 (2020) 105247. https://doi.org/10.1016/j.nanoen.2020.105247.

16. H. Sun, X. Fu, S. Xie, Y. Jiang, H. Peng, Electrochemical capacitors with high output voltages that mimic electric eels, Adv. Mater., 2016, 28, 2070–2076. https://doi.org/10.1002/adma.201505742.

17. M. Liu, B. Li, H. Zhou, C. Chen, Y. Liu, T. Liu, Extraordinary rate capability achieved by a 3D "skeleton/skin" carbon aerogel–polyaniline hybrid with vertically aligned pores, Chem. Commun. 53 (2017) 2810–2813. https://doi.org/10.1039/c7cc00121e.

18. P. Gao, E.V. Rebrov, T.M.W.G.M. Verhoeven, J.C. Schouten, R. Kleismit, G. Kozlowski, J. Cetnar, Z. Turgut, G. Subramanyam, Structural investigations and magnetic properties of sol-gel $Ni_{0.5}Zn_{0.5}Fe_2O_4$ thin films for microwave heating, J. Appl. Phys. 107 (2010) 044317. https://doi.org/10.1063/1.3309767.

19. T.K. Houlding, K. Tchabanenko, M.T. Rahman, E.V. Rebrov, Direct amide formation using radiofrequency heating, Org. Biomol. Chem. 11 (2013) 4171-4177. https://doi.org/10.1039/c2ob26930a.

20. V. Sunny, P. Kurian, P. Mohanan, P.A. Joy, M.R. Anantharaman, A flexible microwave absorber based on nickel ferrite nanocomposite, J. Alloy. Compd. 489 (2010) 297-303. https://doi.org/10.1016/j.jallcom.2009.09.077.

21. R. Jasrotia, V.P. Singh, B. Sharma, A. Verma, P. Puri, R. Sharma, M. Singh, Sol-gel synthesized Ba-Nd-Cd-In nanohexaferrites for high frequency and microwave devices applications, J. Alloys Compd. 830 (2020) 154687. https://doi.org/10.1016/j.jallcom.2020.154687.

22. X. Zhu, X. Wang, K. Liu, M. Meng, M.N. Akhtar, Microwave absorption characteristics of carbon foam decorated with $BaFe_{12}O_{19}$ and $Ni_{0.5}Co_{0.5}Fe_2O_4$ magnetic composite in X-band frequency, J. Magn. Magn. Mater. 513 (2020) 167258. https://doi.org/10.1016/j.jmmm.2020.167258.

23. A.V. Trukhanov, K.A. Astapovich, M.A. Almessiere, V.A. Turchenko, E.L. Trukhanova, V.V. Korovushkin, A.A. Amirov, M.A. Darwish, D.V. Karpinsky, D.A. Vinnik, D.S. Klygach, M.G. Vakhitov, M.V. Zdorovets, A.L. Kozlovskiy, S.V. Trukhanov, Pecularities of the magnetic structure and microwave properties in $Ba(Fe_{1-x}Sc_x)_{12}O_{19}$ (x<0.1) hexaferrites, J. Alloys Compd. 822 (2020) 153575. https://doi.org/10.1016/j.jallcom.2019.153575.

24. V. Turchenko, V.G. Kostishyn, S. Trukhanov, F. Damay, F. Porcher, M. Balasoiu, N. Lupu, B. Bozzo, I. Fina, A. Trukhanov, J. Waliszewski, K. Recko, S. Polosan, Crystal and magnetic

25. structures, magnetic and ferroelectric properties of strontium ferrite partially substituted with In ions, J. Alloys Compd. 821 (2020) 153412. https://doi.org/10.1016/j.jallcom.2019.153412.

25. E.W. Gorter, Some properties of ferrites in connection with their chemistry, Proc. IRE 43 (1955) 1945-1973. https://doi.org/10.1109/jrproc.1955.278060.

26. A.V. Trukhanov, V.O. Turchenko, I.A. Bobrikov, S.V. Trukhanov, I.S. Kazakevich, A.M. Balagurov, Crystal structure and magnetic properties of the $BaFe_{12-x}Al_xO_{19}$ (x=0.1–1.2) solid solutions, J. Magn. Magn. Mater. 393 (2015) 253-259. https://doi.org/10.1016/j.jmmm.2015.05.076.

27. P. Gütlich, A. Hauser, H. Spiering, Thermal and optical switching of Iron(II) complexes , Angew. Chem. Int. Ed. Engl. 33 (1994) 2024-2054. https://doi.org/10.1002/anie.199420241.

28. S.V. Trukhanov, I.O. Troyanchuk, A.V. Trukhanov, I.A. Bobrikov, V.G. Simkin, A.M. Balagurov, Concentration-dependent structural transition in the $La_{0.70}Sr_{0.30}MnO_{3-\delta}$ system, JETP Lett. 84 (2006) 254-257. https://doi.org/10.1134/S002136400617005X.

29. W. Zhang, Y. Bai, X. Han, L. Wang, X. Lu, L. Qiao, Magnetic properties of Co-Ti substituted barium hexaferrite, J. Alloys Compd. 546 (2013) 234-238. https://doi.org/10.1016/j.jallcom.2012.08.029.

30. L. Wang, H. Yu, X. Ren, G. Xu, Magnetic and microwave absorption properties of $BaMn_xCo_{1-x}TiFe_{10}O_{19}$, J. Alloys Compd. 588 (2014) 212-216. https://doi.org/10.1016/j.jallcom.2013.11.072.

31. P. Meng, K. Xiong, L. Wang, S. Li, Y. Cheng, G. Xu, Tunable complex permeability and enhanced microwave absorption properties of $BaNi_xCo_{1-x}TiFe_{10}O_{19}$, J. Alloys Compd. 628 (2015) 75-80. https://doi.org/10.1016/j.jallcom.2014.10.163.

32. S. Verma, O.P. Pandey, A. Paesano Jr., P. Sharma, Structural and magnetic properties of Co-Ti substituted barium hexaferrite thick films, J. Alloys Compd. 678 (2016) 284-289. https://doi.org/10.1016/j.jallcom.2016.03.283.

33. J. Chen, P. Meng, M. Wang, G. Zhou, X. Wang, G. Xu, Electromagnetic and microwave absorption properties of $BaMg_xCo_{1-x}TiFe_{10}O_{19}$, J. Alloys Compd. 679 (2016) 335-340. https://doi.org/10.1016/j.jallcom.2016.04.001.

34. D.S. Klygach, M.G. Vakhitov, D.A. Vinnik, A.V. Bezborodov, S.A. Gudkova, V.E. Zhivulin, D.A. Zherebtsov, C.P. SakthiDharana, S.V. Trukhanov, A.V. Trukhanov, A.Yu. Starikova, Measurement of permittivity and permeability of barium hexaferrite, J. Magn. Magn. Mat. 465 (2018) 290-294. https://doi.org/10.1016/j.jmmm.2018.05.054.

35. Q. Li, Y. Chen, V.G. Harris, Particle-size distribution modified effective medium theory and validation by magneto-dielectric Co-Ti substituted BaM ferrite composites, J. Magn. Magn. Mater. 453 (2018) 44-47. https://doi.org/10.1016/j.jmmm.2018.01.013.

36. R. Sai, M. Sato, S. Takeda, S. Yabukami, M. Yamaguchi, Co/Ti-substituted SrM-based composite sheets: High frequency permeability and electromagnetic noise suppression above 6 GHz, J. Magn. Magn. Mater. 459 (2018) 49-56. https://doi.org/10.1016/j.jmmm.2017.12.051.

37. D.A. Vinnik, D.S. Klygach, V.E. Zhivulin, A.I. Malkin, M.G. Vakhitov, S.A. Gudkova, D.M. Galimov, D.A. Zherebtsov, E.A. Trofimov, N.S. Knyazev, V.V. Atuchin, S.V. Trukhanov, A.V. Trukhanov, Electromagnetic properties of $BaFe_{12}O_{19}$:Ti at centimeter wavelengths, J. Alloys Compd. 755 (2018) 177-183. https://doi.org/10.1016/j.jallcom.2018.04.315.

38. C. Liu, Y. Zhang, Y. Zhang, G. Fang, X. Zhao, K. Peng, J. Zou, Multiple nature resonance behavior of $BaFe_xTiO_{19}$ controlled by Fe/Ba ratio and its regulation on microwave absorption properties, J. Alloys Compd. 773 (2019) 730-738. https://doi.org/10.1016/j.jallcom.2018.09.278.

39. S.B. Narang, A. Arora, Broad-band microwave absorption and magnetic properties of M-type $Ba_{(1-2x)}La_xNa_xFe_{10}Co_{0.5}TiMn_{0.5}O_{19}$ hexagonal ferrite in 18.0–26.5 GHz frequency range, J. Magn. Magn. Mater. 473 (2019) 272-277. https://doi.org/10.1016/j.jmmm.2018.10.042.

40. D.A. Vinnik, V.E. Zhivulin, A.Yu. Starikov, S.A. Gudkova, E.A. Trofimov, A.V. Trukhanov, S.V. Trukhanov, V.A. Turchenko, V.V. Matveev, E. Lahderanta, E. Fadeev, T.I. Zubar, M.V. Zdorovets, A.L. Kozlovsky, Influence of titanium substitution on structure, magnetic and electric properties of barium hexaferrites $BaFe_{12-x}Ti_xO_{19}$, J. Magn. Magn. Mater. 498 (2020) 166117. https://doi.org/10.1016/j.jmmm.2019.166117.

41. H.M. Rietveld, A profile refinement method for nuclear and magnetic structures, J. Appl. Cryst. 2 (1969) 65-71. https://doi.org/10.1107/s0021889869006558.

42. J. Rodriguez-Carvajal, Recent advances in magnetic structure determination by neutron powder diffraction, Phys. B 192 (1993) 55-69. https://doi.org/10.1016/0921-4526(93)90108-i.

43. S.V. Trukhanov, A.V. Trukhanov, V.A. Turchenko, V.G. Kostishyn, L.V. Panina, I.S. Kazakevich, A.M. Balagurov, Structure and magnetic properties of $BaFe_{11.9}In_{0.1}O_{19}$ hexaferrite in a wide temperature range, J. Alloys Compd. 689 (2016) 383-393. https://doi.org/10.1016/j.jallcom.2016.07.309.

44. T. Degen, M. Sadki, E. Bron, U. König, G. Nénert, The HighScore suite, Powder Diffraction 29 (2014) S13-S18. https://doi.org/10.1017/S0885715614000840.

45. http://www.icdd.com/

46. S.V. Trukhanov, A.V. Trukhanov, A.N. Vasiliev, H. Szymczak, Frustrated exchange interactions formation at low temperatures and high hydrostatic pressures in $La_{0.70}Sr_{0.30}MnO_{2.85}$, JETP 111 (2010) 209-214. https://doi.org/10.1134/S106377611008008X.

47. S.V. Trukhanov, A.V. Trukhanov, A.N. Vasiliev, A.M. Balagurov, H. Szymczak, Magnetic state of the structural separated anion-deficient $La_{0.70}Sr_{0.30}MnO_{2.85}$ manganite. JETP 113 (2011) 819-825. https://doi.org/10.1134/S1063776111130127.

48. S.V. Trukhanov, A.V. Trukhanov, M.M. Salem, E.L. Trukhanova, L.V. Panina, V.G. Kostishyn, M.A. Darwish, An.V. Trukhanov, T.I. Zubar, D.I. Tishkevich, V. Sivakov, D.A. Vinnik, S.A. Gudkova, Charanjeet Singh, Preparation and investigation of structure, magnetic and dielectric properties of $(BaFe_{11.9}Al_{0.1}O_{19})_{1-x}$ - $(BaTiO_3)_x$ bicomponent ceramics, Ceram. Int. 44 (2018) 21295-21302. https://doi.org/10.1016/j.ceramint.2018.08.180.

49. R.D. Shannon, Revised effective ionic radii and systematic studies of interatomic distances in halides and chalcogenides, Acta Crystallogr. A 32 (1976) 751-767. https://doi.org/10.1107/s0567739476001551.

50. S.V. Trukhanov, A.V. Trukhanov, H. Szymczak, Effect of magnetic fields on magnetic phase separation in anion-deficient manganite $La_{0.70}Sr_{0.30}MnO_{2.85}$, Low Temp. Phys. 37 (2011) 465-469. https://doi.org/10.1063/1.3614412.

51. C.P. Bean, J.D. Livingstone, Superparamagnetism, J. Appl. Phys. 30 (1959) S120-S129. https://doi.org/10.1063/1.2185850.

52. N. Paradis, G. Chastanet, J.-F. Létard, When stable and metastable HS states meet in spin-crossover compounds, Eur. J. Inorg. Chem. 2012 (2012) 3618-3624. https://doi.org/10.1002/ejic.201200297.

53. N. Paradis, G. Chastanet, T. Palamarciuc, P. Rosa, F. Varret, K. Boukheddaden, J.-F. Létard, Detailed investigation of the interplay between the thermal decay of the low temperature metastable HS state and the thermal hysteresis of spin-crossover solids, J. Phys. Chem. C 119 (2015) 20039-20050. https://doi.org/10.1021/acs.jpcc.5b03680.

Figure captions

Fig. 1. X-ray diffraction patterns and their Rietveld refinement for the $BaFe_{12-x}Ti_xO_{19}$ samples with x = 0.25 (left panel); 1.00 (central panel) and 2.00 (right panel) at T = 100 K (a, d, j); 300 K (b, e, h) and 900 K (c, f, i). The crosses show the experimental data. The top red solid line is a fitting curve. The bottom blue line is a difference curve. Vertical bars define the Bragg's positions.

Fig. 2. Concentration dependence of lattice constant a (a), lattice constant c (b) and volume V (c) of unit cell at T = 100 K (black circles); 300 K (red circles) and 900 K (green circles) for the $BaFe_{12-x}Ti_xO_{19}$ samples.

Fig. 3. Temperature dependence of lattice constant a (a), lattice constant c (b) and volume V (c) of unit cell for the $BaFe_{12-x}Ti_xO_{19}$ samples with x = 0.25 (black circles); 1.00 (red circles) and 2.00 (green circles).

Fig. 4. Temperature dependence of ZFC (open circles) and FC (full circles) magnetization in field of 0.01 T for the $BaFe_{12-x}Ti_xO_{19}$ samples with x = 0.25 (black circles); 0.50 (red circles); 1.00 (green circles) and 1.50 (blue circles). Insert demonstrate linear fitting of the T_{dif} difference temperature in field of 0.01 T.

Fig. 5. Temperature dependence of derivative of ZFC magnetization in field of 1 T for the $BaFe_{12-x}Ti_xO_{19}$ samples with x = 0.25 (black line); 0.50 (red line); 1.00 (green line) and 1.50 (blue line). Insert demonstrate polinomial fitting of the T_{inf} inflection point temperature for the ZFC magnetization in field of 0.01 T for the same samples.

Fig. 6. Temperature dependence of ZFC (open circles) and FC (full circles) magnetization in field of 1 T for the $BaFe_{12-x}Ti_xO_{19}$ samples with x = 0.25 (black circles); 0.50 (red circles); 1.00 (green circles) and 1.50 (blue circles). Insert demonstrate linear fitting of the T_{dif} difference temperature in fields of 0.01 T and 1 T.

Fig. 7. Temperature dependence of magnetization in field of 2 T for the $BaFe_{12-x}Ti_xO_{19}$ samples with x = 1.00 (black circles) and 1.50 (red circles).

Fig. 8. Field dependence of magnetization at room temperature for the $BaFe_{12-x}Ti_xO_{19}$ samples with x = 0.00 (black circles); 0.25 (red circles); 0.50 (green circles); 0.75 (blue circles); 1.00 (cyan circles); 1.25 (magneta circles); 1.50 (dark yellow circles); 1.75 (purple circles) and 2.00 (wine circles).

Fig. 9. Field dependence of magnetization at room temperature for the $BaFe_{12-x}Ti_xO_{19}$ samples with x = 0.00 (black circles); 0.25 (red circles); 0.50 (green circles); 0.75 (blue circles); 1.00 (cyan circles); 1.25 (magneta circles); 1.50 (dark yellow circles); 1.75 (purple circles) and 2.00 (wine circles) in range of ±50 mT.

Fig. 10. Typical ESR spectrum for the $BaFe_{12-x}Ti_xO_{19}$ sample with x = 1.50 at X-band frequency in the temperature range of 292 – 678 K.

Fig. 11. Temperature dependence of the integral intensity of ESR lines for the $BaFe_{12-x}Ti_xO_{19}$ sample with x = 1.50. Inset shows the first derivative of the integral intensity with respect to temperature dI_{int}/dT.

Fig. 12. Concentration dependence of the M_S spontaneous magnetization (a); M_r residual magnetization (b) and B_C coercivity (c) for the $BaFe_{12-x}Ti_xO_{19}$ samples at room temperature.

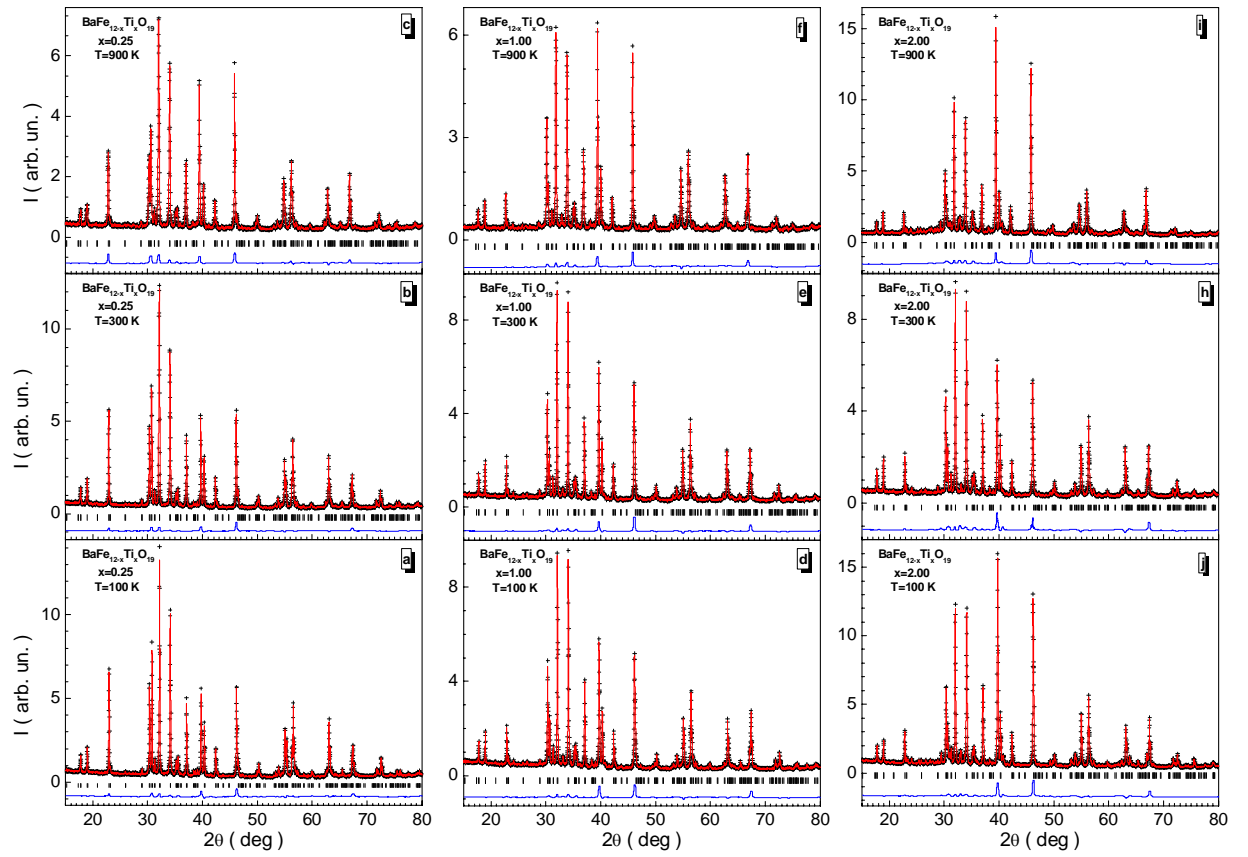Fig. 1. X-ray diffraction patterns and their Rietveld refinement for the BaFe$_{12-x}$Ti$_x$O$_{19}$ samples with x = 0.25 (left panel); 1.00 (central panel) and 2.00 (right panel) at T = 100 K (a, d, j); 300 K (b, e, h) and 900 K (c, f, i). The crosses show the experimental data. The top red solid line is a fitting curve. The bottom blue line is a difference curve. Vertical bars define the Bragg's positions.
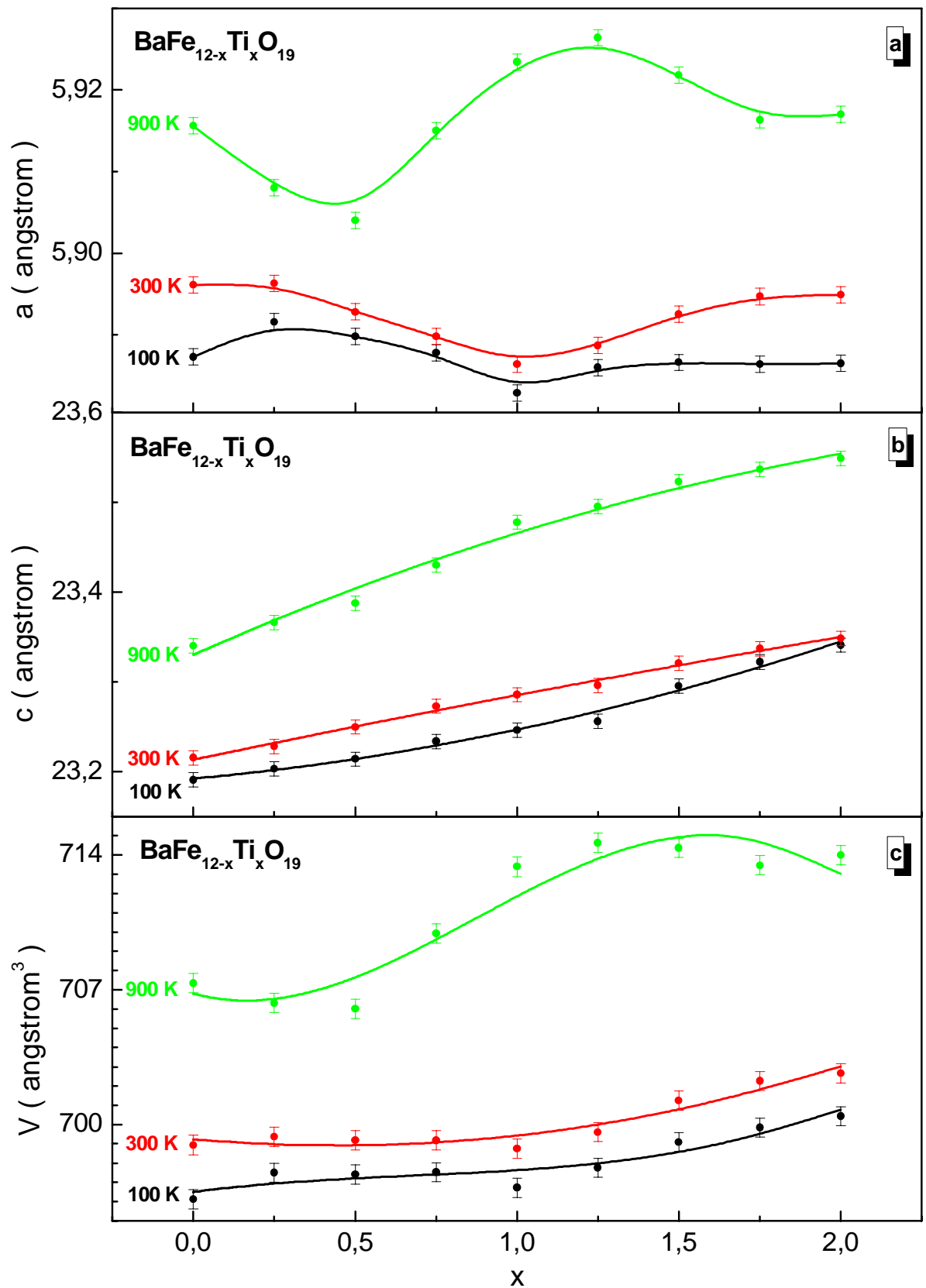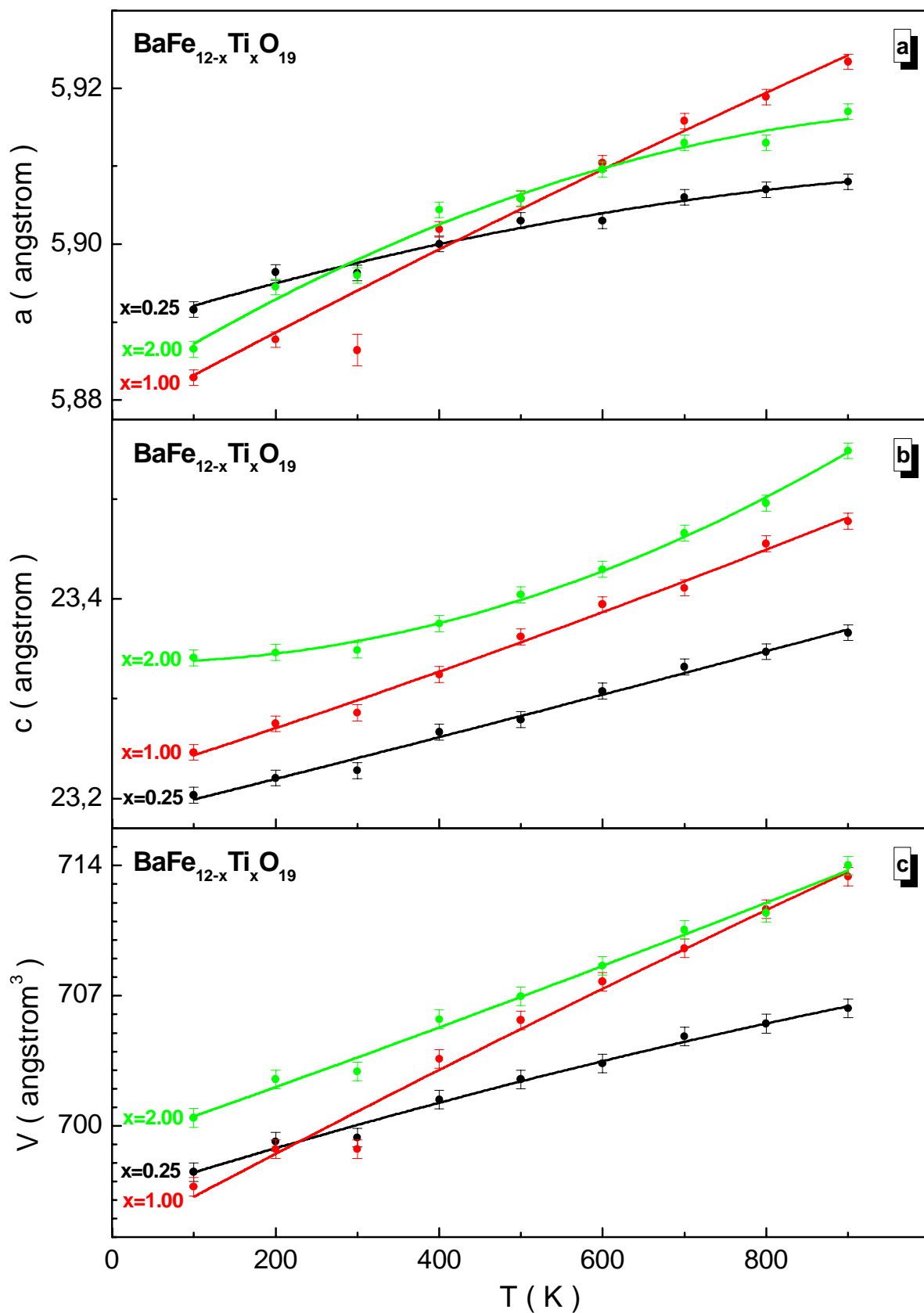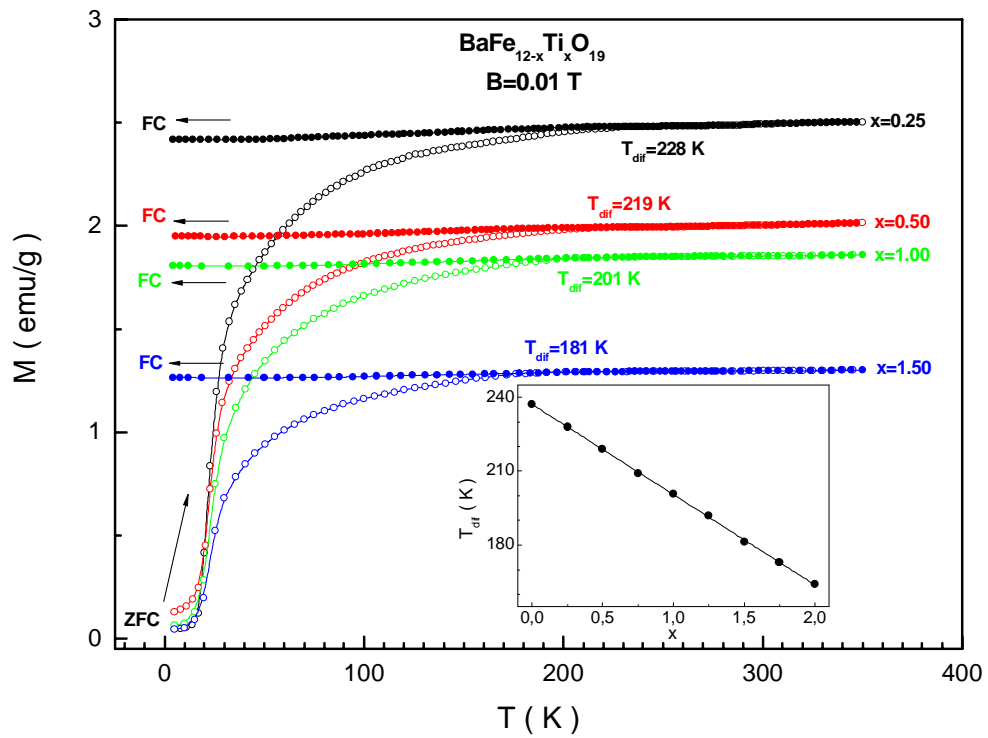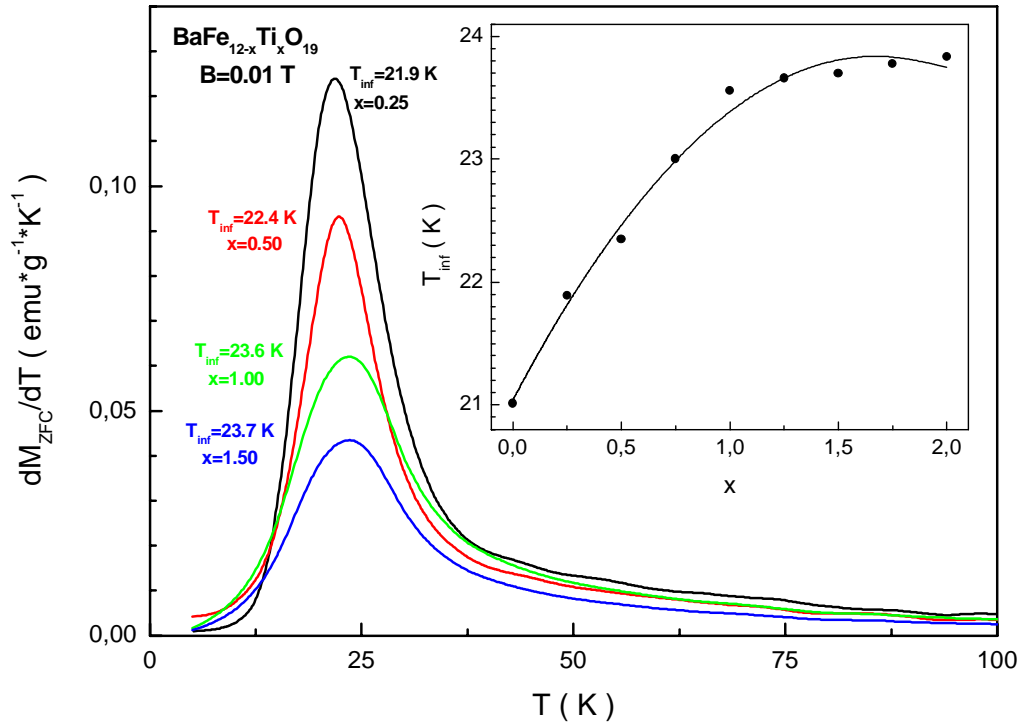
Fig. 2. Concentration dependence of a parameter (a), c parameter (b) and V volume (c) of unit cell at T = 100 K (black circles); 300 K (red circles) and 900 K (green circles) for the BaFe$_{12-x}$Ti$_x$O$_{19}$ samples.

Fig. 3. Temperature dependence of a parameter (a), c parameter (b) and V volume (c) of unit cell for the $BaFe_{12-x}Ti_xO_{19}$ samples with x = 0.25 (black circles); 1.00 (red circles) and 2.00 (green circles).
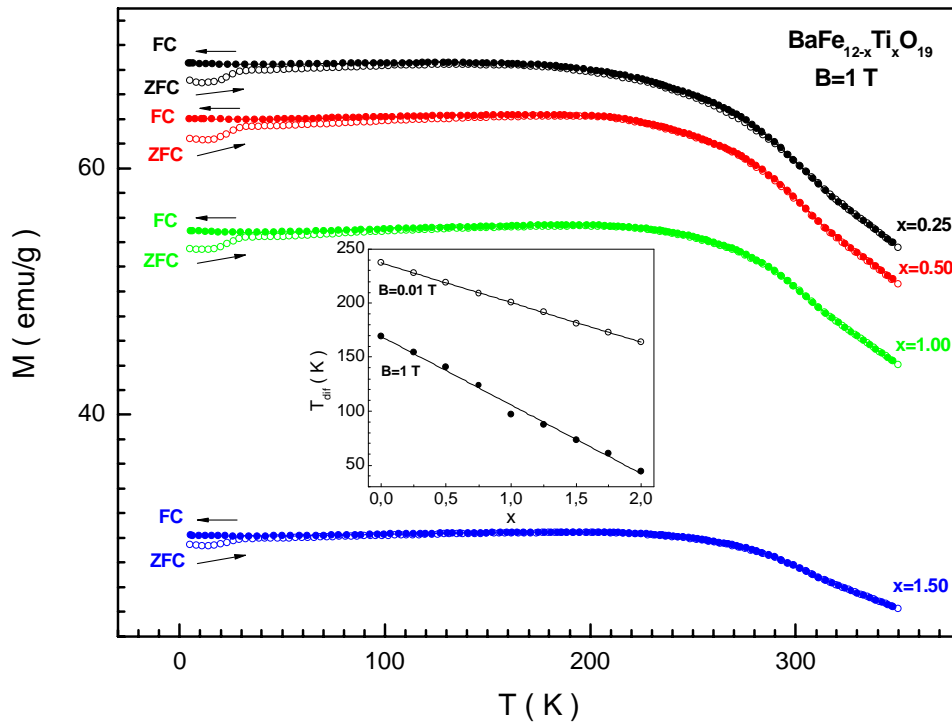
Fig. 4. Temperature dependence of ZFC (open circles) and FC (full circles) magnetization in field of 0.01 T for the $BaFe_{12-x}Ti_xO_{19}$ samples with x = 0.25 (black circles); 0.50 (red circles); 1.00 (green circles) and 1.50 (blue circles). Insert demonstrate linear fitting of the T_{dif} difference temperature in field of 0.01 T.
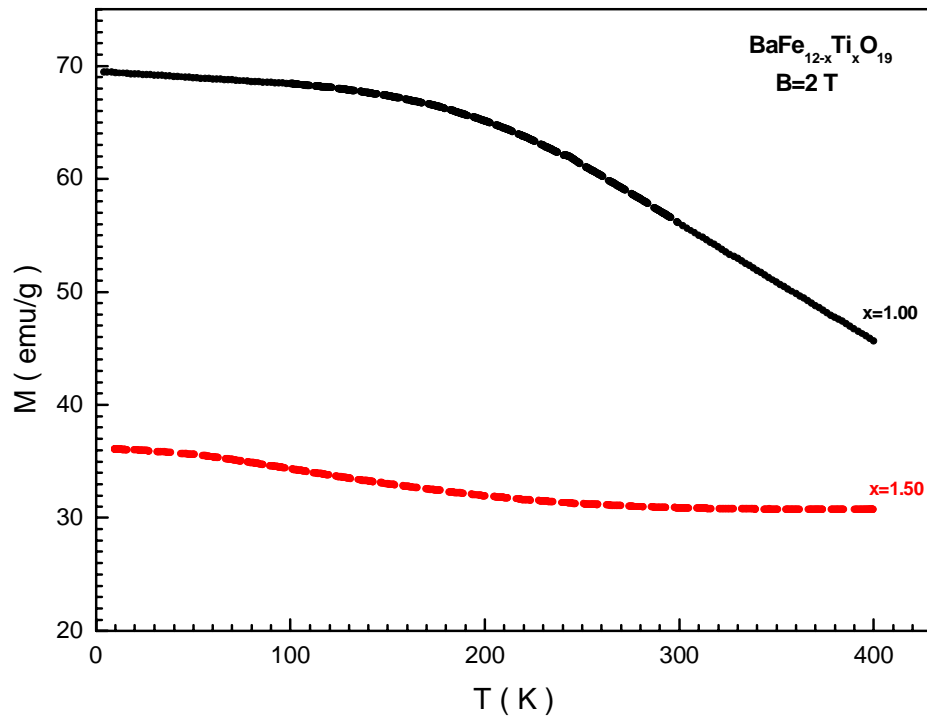
Fig. 5. Temperature dependence of derivative of ZFC magnetization in field of 1 T for the BaFe$_{12-x}$Ti$_x$O$_{19}$ samples with x = 0.25 (black line); 0.50 (red line); 1.00 (green line) and 1.50 (blue line). Insert demonstrate polinomial fitting of the T$_{inf}$ inflection point temperature for the ZFC magnetization in field of 0.01 T for the same samples.

Fig. 6. Temperature dependence of ZFC (open circles) and FC (full circles) magnetization in field of 1 T for the $BaFe_{12-x}Ti_xO_{19}$ samples with x = 0.25 (black circles); 0.50 (red circles); 1.00 (green circles) and 1.50 (blue circles). Insert demonstrate linear fitting of the T_{dif} difference temperature in fields of 0.01 T and 1 T.

Fig. 7. Temperature dependence of magnetization in field of 2 T for the $BaFe_{12-x}Ti_xO_{19}$ samples with x = 1.00 (black circles) and 1.50 (red circles).

Fig. 8. Field dependence of magnetization at room temperature for the $BaFe_{12-x}Ti_xO_{19}$ samples with x = 0.00 (black circles); 0.25 (red circles); 0.50 (green circles); 0.75 (blue circles); 1.00 (cyan circles); 1.25 (magneta circles); 1.50 (dark yellow circles); 1.75 (purple circles) and 2.00 (wine circles).
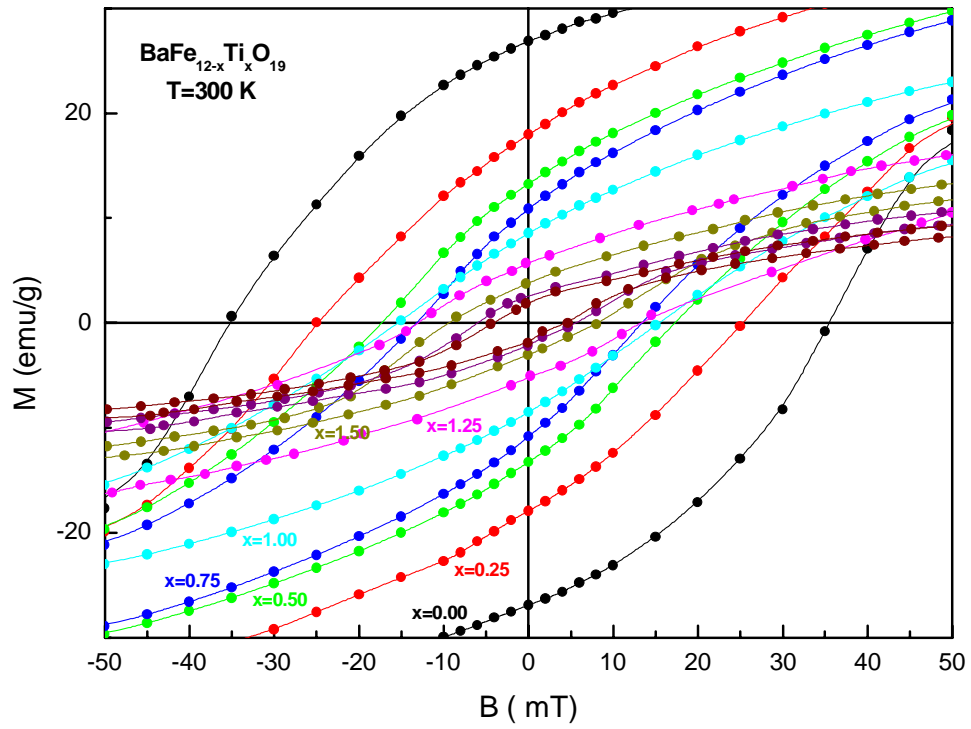
Fig. 9. Field dependence of magnetization at room temperature for the $BaFe_{12-x}Ti_xO_{19}$ samples with x = 0.00 (black circles); 0.25 (red circles); 0.50 (green circles); 0.75 (blue circles); 1.00 (cyan circles); 1.25 (magneta circles); 1.50 (dark yellow circles); 1.75 (purple circles) and 2.00 (wine circles) in range of ±50 mT.
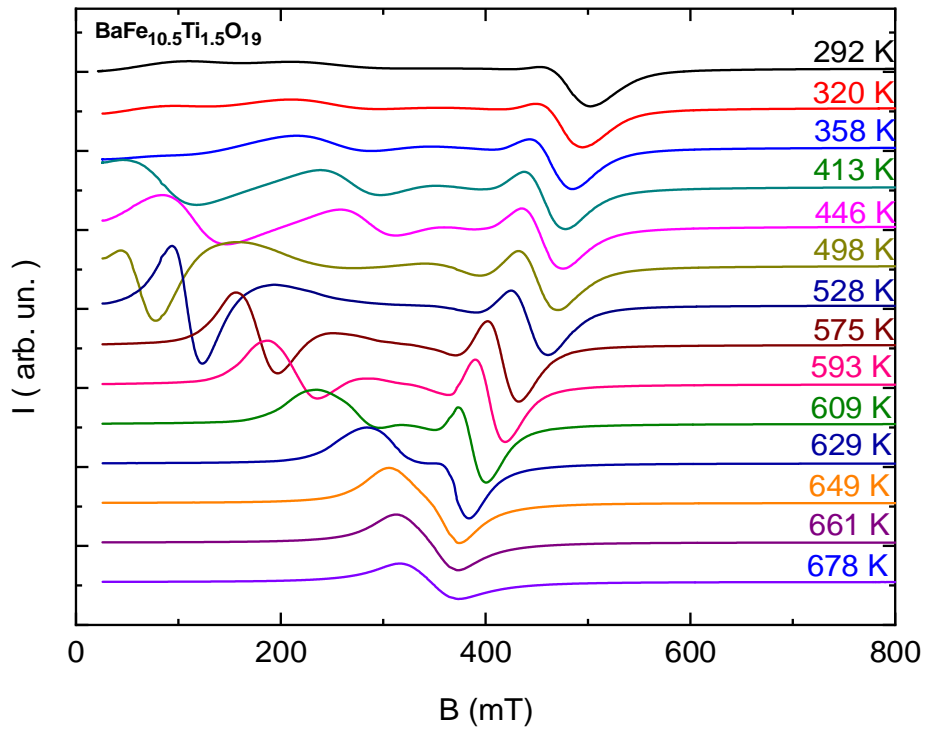
Fig. 10. Typical ESR spectrum for the $BaFe_{12-x}Ti_xO_{19}$ sample with x = 1.50 at X-band frequency in the temperature range of 292 – 678 K.
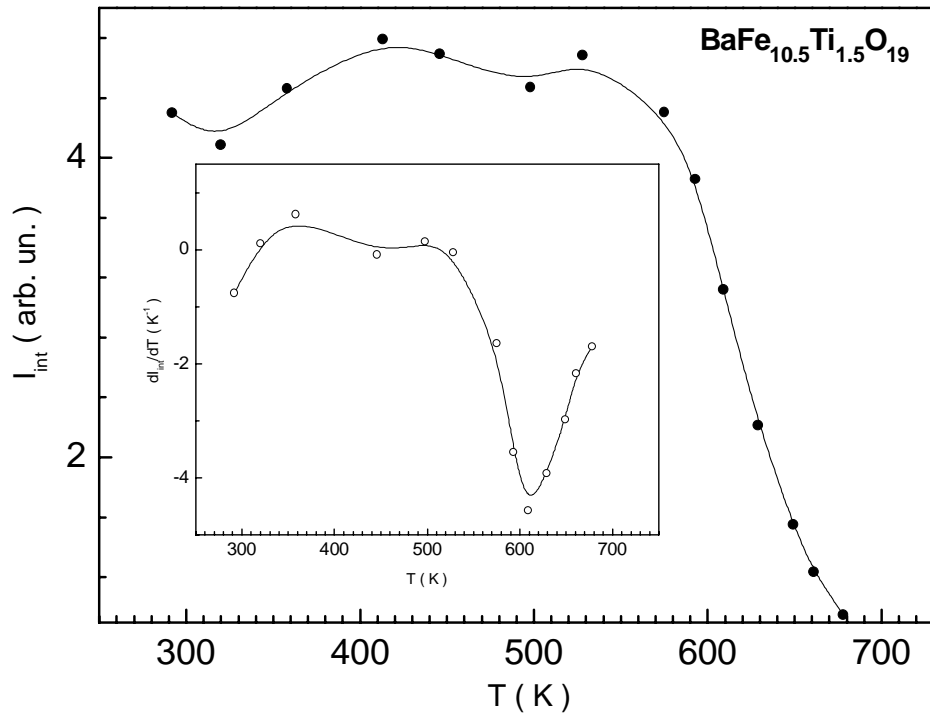
Fig. 11. Temperature dependence of the integrated intensity of EPR spectrum for the $BaFe_{12-x}Ti_xO_{19}$ sample with x = 1.50.
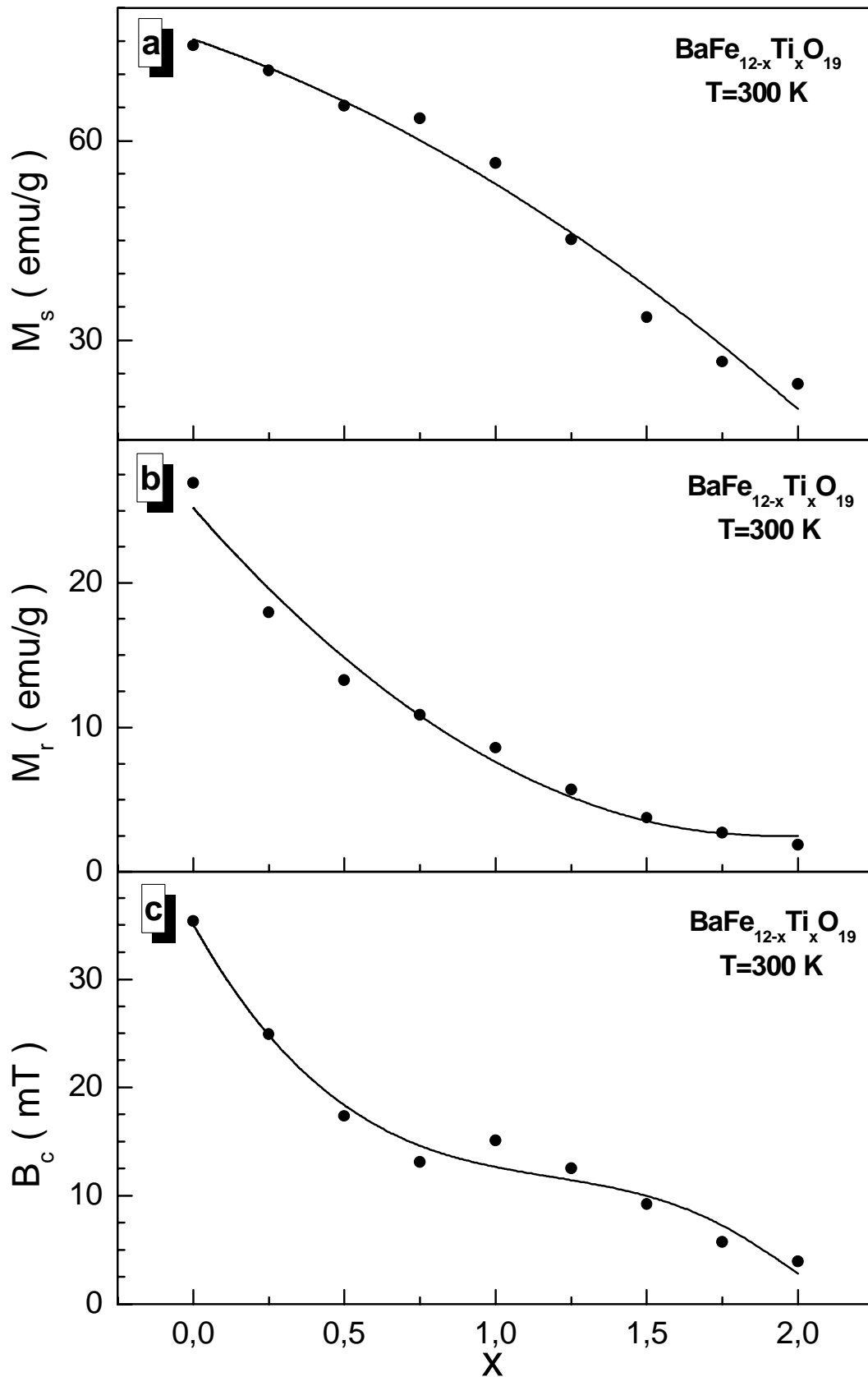
Fig. 12. Concentration dependence of the M_S spontaneous magnetization (a); M_r residual magnetization (b) and B_C coercivity (c) for the $BaFe_{12-x}Ti_xO_{19}$ samples at room temperature.